Yang *et al. Journal of Nanobiotechnology* (2025) 23:267
https://doi.org/10.1186/s12951-025-03320-2

Journal of Nanobiotechnology

RESEARCH **Open Access**

Closed-loop cascade nanozyme strategy for mutually reinforced catalytic and mild-temperature photothermal therapeutic effects

Fan Yang[1,2†], Chunyu Yan[1†], Nannan Li[1†], Xinxiu Jiang[1], Baojie Du[2], Peirong Bai[2], Liping Li[1*] and Ruiping Zhang[3*]

Abstract
Nanocatalysis coupled with photothermal therapy is a potent anti-cancer approach, yet its clinical utility is limited by low concentration of tumor substrate, redox interference, and risks of overheating normal tissues. Herein, we propose an innovative closed-loop nanozyme approach that leverages the synergistic effects of catalytic and mild photothermal therapy (mPTT) to address aforementioned challenges. The strategy features a folic acid-functionalized iron single-atom catalyst (FeNC-FA), designed to exhibit exceptional multienzymatic capabilities and an optimal photothermal response. In the system, the engineered FeNC-FA is capable of inducing reactive oxygen species (ROS) storm and depleting glutathione (GSH) in the specific tumor microenvironment (TME) to initiate ferroptosis. Concurrently, the accumulation of ROS effectively cleaves heat shock proteins (HSPs), thereby enhancing mPTT. An intriguing aspect is that the increased temperature within the TME further facilitates the conversion of H_2O_2 to O_2, alleviating hypoxia and providing a positive feedback circuit to boost catalytic therapy. Additionally, the advanced photoacoustic (PA) imaging capabilities of FeNC-FA allow for self-monitoring of their accumulation at tumor sites, thereby guiding the mPTT process. Taken together, it provides a PA image-guided, mutually reinforced catalytic and mild photothermal synergistic tumor therapy both in vitro and in vivo. This targeted and synergistic strategy holds great promise for personalized medicine applications.

Keywords Single-atom nanozyme, Nanocatalytic therapy, PA imaging guided-synergistic therapy, Mild-temperature photothermal therapy, Closed-loop strategy

Introduction

Reactive oxygen species (ROS), a class of intracellular signaling molecules and metabolites, are responsible for the regulation of physiological functions [1]. Extensive investigations have revealed that excess ROS can break the dynamic balance between the oxidized and reduced state in the tumor microenvironment (TME), resulting in irreversible cell oxidative damage and apoptosis [2, 3, 4]. Currently, therapeutic approaches such as photodynamic therapy (PDT) [5, 6, 7, 8, 9], sonodynamic therapy (SDT) [10, 11, 12, 13], and nanozyme-mediated catalytic therapy (NCT) have gained prominence in cancer treatment due to their efficient ROS generation with minimized

---

†Fan Yang, Chunyu Yan and Nannan Li contributed equally to this work.

*Correspondence:
Liping Li
liliping_8103@163.com
Ruiping Zhang
zrp_7142@sxmu.edu.cn
[1] Basic Medical College, Research Institute of Circadian Rhythm and Disease, Academy of Medical Sciences, Shanxi Medical University, Taiyuan 030001, China
[2] Shanxi Bethune Hospital, Third Hospital of Shanxi Medical University, Shanxi Academy of Medical Sciences, Tongji Shanxi Hospital, Taiyuan 030032, China
[3] The Radiology Department of Shanxi Provincial People's Hospital, Five Hospital of Shanxi Medical University, Taiyuan 030001, China

side effects [14, 15]. Notably, NCT stands out as a highly promising cancer treatment strategy because it generates ROS via catalytic reactions that utilize endogenous substances, thereby eliminating the need for external activation [16, 17]. However, the low catalytic efficiency of nanozymes, attributed to the lack of active sites, restricts their application in NCT and other fields [18, 19, 20, 21, 22]. Moreover, their susceptibility to high levels of glutathione (GSH) in the TME further complicates their use in NCT [23, 24].

More recently, single-atom nanozymes (SAzymes) featuring independently dispersed metal atom active sites, have received extensive attention in biosensor and biomedicine field [25–27]. Benefiting from unique geometric and electronic structure, SAzymes own the maximum atom utilization rate and exhibit a more powerful enzyme mimetic catalytic activity than the conventional nanozymes, even superior to that of natural enzymes [28, 29]. Iron (Fe), a common cofactor in various metalloenzymes essential to life processes, has been a focus of interest since the discovery of Fe_3O_4 nanoparticles as peroxidase (POD) mimics in 2007, spurring a surge of research into the development of Fe-based SAzymes [30, 31]. The multifunctional Fe SAzyme with various enzymatic activities has been documented, especially GSH oxidase (GSHOx)-like activities, benefiting for enhanced ROS production [32]. For example, Qu and co-workers developed a self-adaptive ferroptosis platform by assembling DNA modulators on Fe SAzymes, that enabled the specific enhancement of reactive oxygen species (ROS) generation and on-demand consumption of glutathione (GSH) in tumor cells [33]. Nonetheless, the optimal performance of these catalytic reactions may be hindered by the limited availability of tumor substrates within the TME, such as oxygen. The photothermal effect is usually harnessed to enhance the catalytic activity of NCT and improve local oxygen production [34]. Consequently, the integration of NCT with photothermal therapy has emerged as a potent anti-cancer strategy. Nevertheless, conventional photothermal therapy may inadvertently harm adjacent normal tissues due to heat diffusion [35]. To address this, mild-temperature photothermal therapy (mPTT, 38–43 ℃) has been adopted for synergistic treatment [36, 37]. To our knowledge, the synergistic approaches integrating catalytic therapy with mPTT have typically involved one-directional enhancement, lacking a mutually amplification effect.

Inspired by all these points in mind, we herein proposed a mutually reinforced closed-loop therapeutic strategy that integrated catalytic therapy and mPTT. The Fe-based SAzyme (FeNC) was synthesized by pyrolysis ZIF-8 encapsulated iron precursor (denoted as Fe@ZIF-8, Fig. 1). It exhibited a range of enzyme-like activities, including POD, oxidase (OXD), catalase (CAT), and GSHOx activities. After decorating with folic acid (FA), the FeNC-FA exhibited the cancer cell targeting ability and good biocompatibility. As shown in Fig. 1, a good photoacoustic (PA) imaging capability to monitor FeNC-FA accumulation in tumor region was demonstrated. The FeNC-FA mimicked POD, CAT, and OXD in TME, resulting in plentiful ·OH and $\cdot O_2^-$ generation by the parallel-cascade catalytic reaction. Meanwhile, the FeNC-FA eliminated GSH to further disrupt redox homeostasis and initiate ferroptosis. Subsequently, the accumulation of ROS directly destroyed the structure and function of the up-regulation stress-induced heat shock proteins (HSPs), thereby impeding the repair of heat-induced damage and significantly enhancing mPTT. Moreover, a robust generation of O_2 was achieved, establishing a beneficial positive feedback circuit. It not only effectively alleviated hypoxia within TME, but also improved the effectiveness of NCT. Taken together, the FeNC-FA under a NIR irradiation orchestrated the enzymatic activities realized an amplifying catalytic-mild photothermal synergistic therapy both in vitro and in vivo.

Results and discussion

Synthesis and characterization of FeNC-FA

The detailed synthesis and modification procedure of FeNC was illustrated in Fig. 2a. Initially, the ZIF-8 encapsulated iron precursor (Fe@ZIF-8) was self-assembled in the methanol mixture of zinc nitrate hexahydrate, iron acetylacetonate, and dimethylimidazole (2-MI) (Fig. 2b). Then, the pyrolysis process of Fe@ZIF-8 powder was implemented at 1000 ℃ under a N_2 atmosphere. During the procedure, the Zn^{2+} was reduced to its zero-valent state and evaporated, while the organic ligands were carbonized, ultimately yielding the FeNC [38]. A reference samples (named N-C) without Fe-doping was also synthesized by the same strategy. The transmission electron microscopy (TEM, Fig. 2c) and scanning electron microscopy (SEM, Fig. S1) image revealed the rhombic dodecahedron morphology. The energy dispersive X-ray spectroscopy (EDS) analysis clarified the homogeneous distributions of Fe, C, and N in the FeNC (Fig. 2d). The aberration-corrected high-angle annular dark-field scanning transmission electron microscopy (HAADF-STEM) image exhibited abundant bright dots highlighted by red circles, demonstrating the presence of the atomically dispersed Fe over the entire architecture (Fig. 2e). The Fe concentration in the FeNC was 0.12 wt% via inductively coupled plasma optical emission spectrometry (ICP-OES). The X-ray diffraction (XRD) analysis determined that no metallic Fe crystalline peaks in FeNC, and two broad diffraction peaks ascribed to the (101) and (002) of amorphous graphitic carbon (Fig. 2f) [37, 39, 40]. The intensity ratio (I_D/I_G) of FeNC and N-C that represents the carbon deficiency were 1.063 and 0.959 (Fig. 2g)

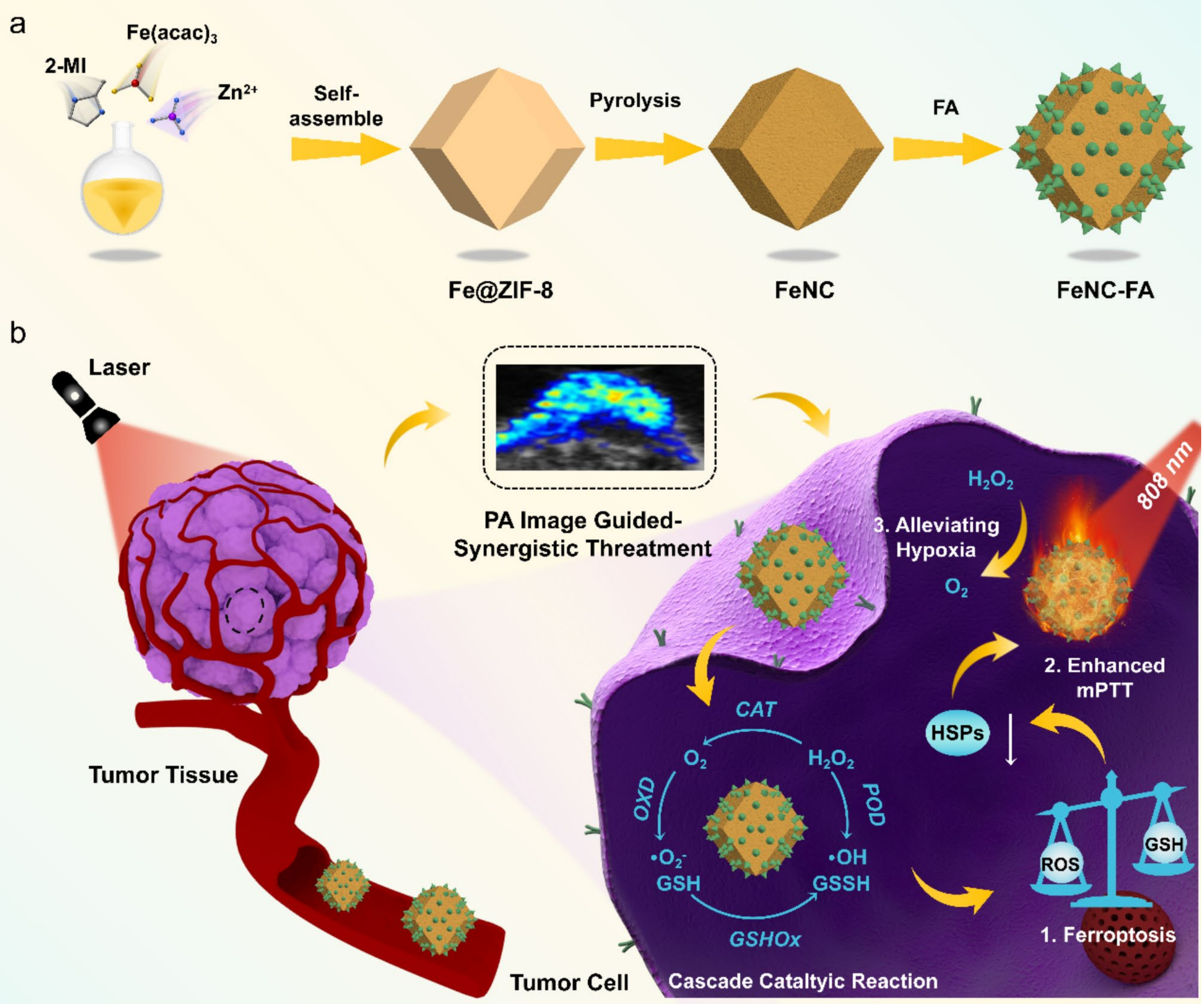

Fig. 1 (**a**) Fabrication route of FeNC-FA. (**b**) The mechanism of PA image guided catalytic-mild temperature photothermal synergistic strategy

from the Raman spectrum, respectively, suggesting a more plentiful defect site with Fe dope [41, 42]. The N_2 adsorption-desorption isotherm revealed the microporous and mesoporous structure of FeNC and their surface area was about 1397 m^2/g (Fig. S2), which supplied a large surface area for rapid diffusion and transportation of reactive species during nanozyme catalysis procedure. The X-ray photoelectron spectroscopy (XPS) spectrum revealed the coexistence of pyridinic N (397.6 eV), pyrrolic N (400.2 eV), and graphitic N (402.3 eV), and oxidized pyridinic N (403.8 eV) (Fig. 2h), and an additional peak at 398.6 eV indicated the Fe-N coordination [43, 44].

To elucidate the local chemical states and atomic coordination of Fe atoms in the FeNC, X-ray absorption near-edge structure (XANES) and Fourier-transformed k^3-weighted extended XAFS (FT-EXAFS) measurements were carried out with iron phthalocyanine (FePc), Fe_2O_3, and Fe foil as reference samples. The XANES spectra exhibited that the rising-edge position of FeNC was between Fe_2O_3 and Fe foil, and relatively close to FePc, implying a positive charge of Fe with a valence state between Fe(II) and Fe(III) (Fig. 3a). The XANES pre-edge peak at 7113 eV and 7113.5 eV was observed in the spectrum of FeNC and FePc, respectively, indicating the presence of Fe-N_4 coordination in FeNC [45]. FT-EXAFS spectra showed a main peak for FeNC at 1.53 Å (Fig. 3b), which corresponded to the Fe-N bond indicated in FePc, while none of the peaks belonging to Fe-Fe peaks (2.2 Å) was observed, suggesting that Fe species was primarily dispersed as single atoms in FeNC. Wavelet transform (WT) of Fe K-edge EXAFS oscillations were implemented (Fig. 3d). The WT contour plots of FeNC revealed one of the major feature centers (5.5 Å^{-1}, 1.5 Å), which ascribed to the Fe-N bonding, and no Fe-Fe signal was detected [46–48]. The least-square EXAFS fittings spectra (Fig. 3c,

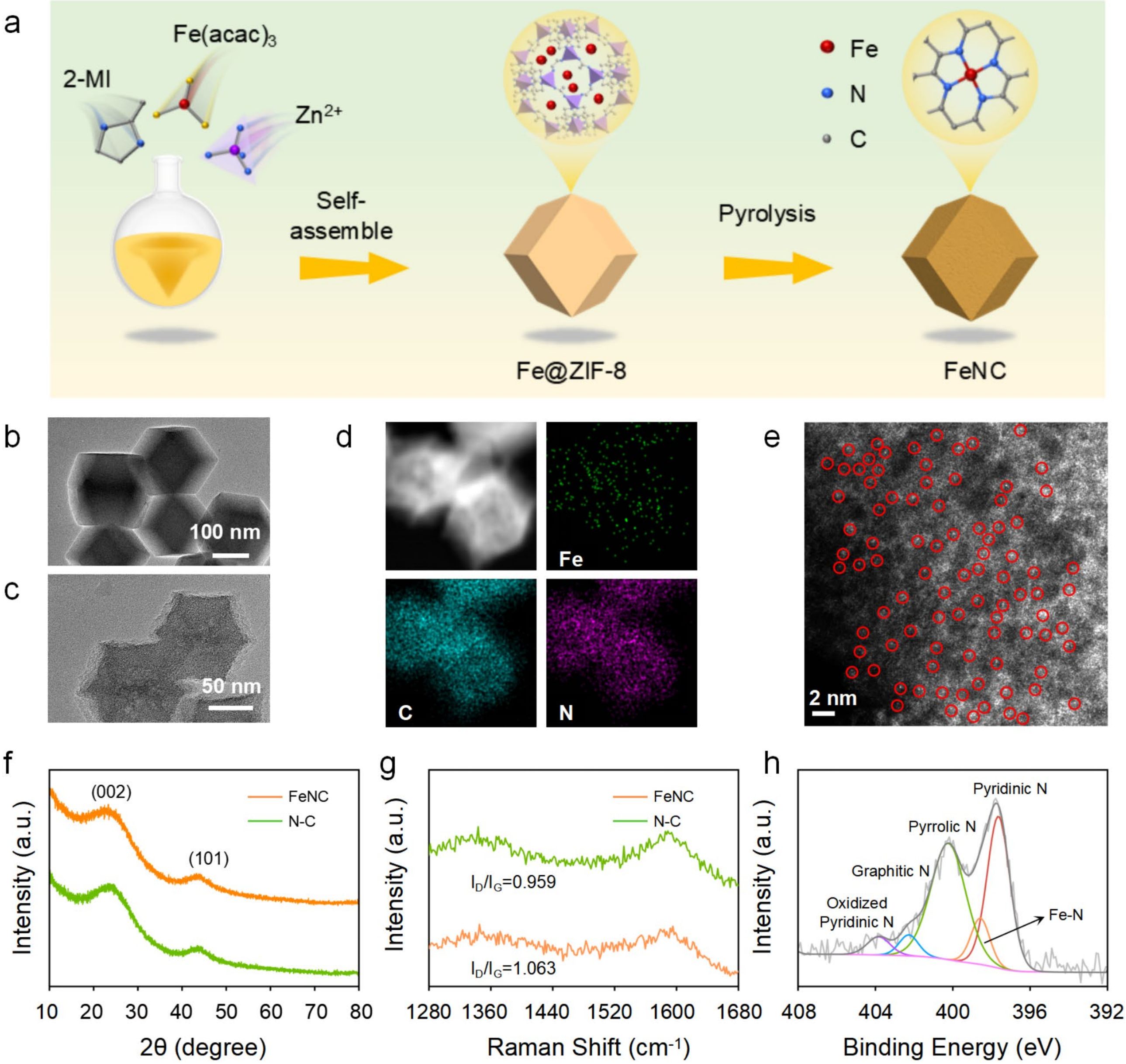

Fig. 2 Characterization of FeNC. (**a**) Schematic diagram of synthetic procedure for FeNC. TEM image of (**b**) Fe@ZIF-8 and (**c**) FeNC. (**d**) EDS mapping images of FeNC. (**e**) HAADF-STEM image of FeNC. (**f**) Powder XRD of FeNC and N-C. (**g**) Raman spectrum of FeNC and N-C. (**h**) High-resolution N 1s XPS spectrum of FeNC

Fig. S3, and Table S1) suggested that the coordination number of Fe-N was 4.1 with a length of 1.98 Å.

Multienzyme mimetic activities of FeNC

The intrinsic multienzyme mimetic activities of FeNC were investigated by relevant experiments (Fig. 4a). The POD-like activity of FeNC was proved by employing 3,3',5,5'-tetramethylbenzidine (TMB) as the chromogenic substrate (Fig. S4), which exhibited a significant absorption peak at 652 nm upon being oxidized by ·OH (Fig. 4b). The electron spin resonance (ESR) spectra with a typical ·OH characteristic peak (1:2:2:1) was trapped in Fig. S5. The typical Michaelis-Menten curves for TMB and H_2O_2 substrates were calculated as previously reported [49]. The K_m values and maximum reaction rates (V_{max}) were 0.64 mM and 15.05×10^{-6} M/min for TMB (Fig. S6b and Table S2), and 24.76 mM and 37.03×10^{-6} M/min for H_2O_2 (Fig. S6e), respectively. The catalytic kinetic parameters of FeNC were compared with those of Fe_3O_4, horseradish peroxidase (HRP), and other catalysts (Table S3), and the results indicated that FeNC exhibited superior performance. The OXD-like activity of FeNC was proved by TMB assay (Fig. S7). An obvious absorption peak at 652 nm was observed in the FeNC + TMB group in the air

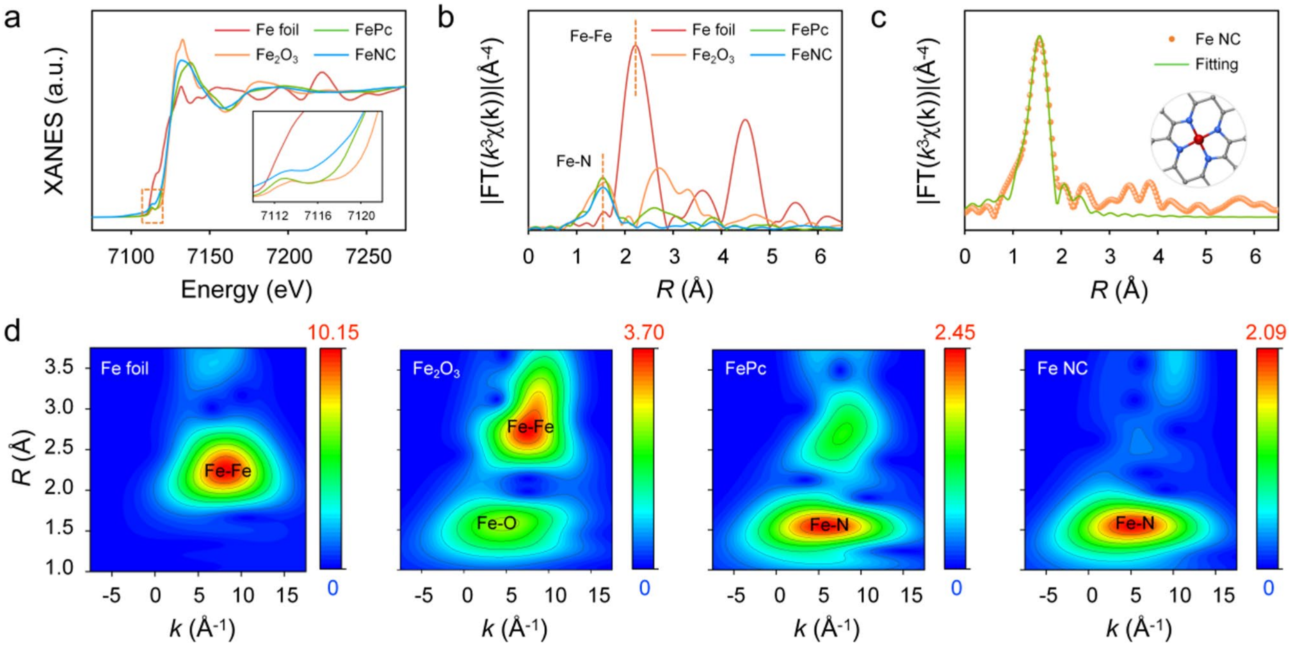

Fig. 3 Atomic structure characterization of FeNC. (**a**) XANES spectra (**b**) FT-EXAFS spectra of the FeNC and reference samples. (**c**) EXAFS R-space fitting curves of the FeNC (Inset: the schematic architectures of FeNC). (**d**) WT-EXAFS contour plots of FeNC and reference samples

(Fig. 4c), while a decreased sharply in the N_2-saturated conditions (Fig. S8). The production of $\cdot O_2^-$ was revealed by ESR spectra (Fig. S5) and commercial detection kit (Fig. S9). It proved that the production of $\cdot O_2^-$ was dependent on the concentration of FeNC. The conversion of TMB by FeNC followed the Michaelis-Menten process with K_m and V_{max} of 0.20 mM and 5.51×10^{-6} M/min, respectively (Fig. S6h and Table S4). The catalytic kinetic parameters of FeNC were compared with those of other nanozymes in Table S5, highlighting its highly efficient and superior OXD-like activity. Subsequently, FeNC exhibited a higher POD (Fig. S10a) and OXD (Fig. S10b) mimic activities than Fe@ZIF-8 and N-C, implying that the catalytic activities were highly dependent on Fe active centers. We further optimized the pyrolysis temperature and obtained Fe-N_x-C under 900 and 1100 °C, respectively. Their relative POD/OXD-like activities (Fig. S11) and Michaelis-Menten kinetics parameters were compared (Fig. 4d and Fig. S6). The FeNC obtained at 1000 °C exhibited superior POD and OXD mimetic activities and was employed for subsequent investigations.

We further investigated the CAT-like activity of FeNC, N-C, and Fe@ZIF-8 (Fig. 4e and Fig. S10c). The content of dissolved oxygen in the FeNC group exhibited a noticeable increase in the presence of H_2O_2. To further increase oxygen production, the photothermal performance of FeNC was investigated (Fig. 4g). The absorption from ultraviolet to the NIR region increased accordingly with the concentration of FeNC, and a laser at 808 nm was utilized for the following experiments (Fig. S12). The temperature of the FeNC aqueous solution raised quickly with the increasing of concentration (Fig. 4h) and irradiation power density (Fig. 4i). The FeNC solution was exposed to laser for 5 min (laser on), and then the laser was switched off (laser off) until the solution was cool to room temperature. The laser on/off repetitions were executed for another four times. The continuous changes of temperature were observed in Fig. S13, indicating the excellent photothermal stability of the FeNC. The photothermal conversion efficiency of FeNC was calculated to be 25.7% (Fig. S14). As expected, a lot of oxygen was observed (Fig. 4e and Fig. S15) even in an acid buffer upon 808 nm laser irradiation.

GSH plays a significant role in the ferroptosis pathway. Briefly, the depletion of GSH would result in glutathione peroxidase 4 (GPX4) inactivation, further lead to LPO up-regulation for ferroptosis initiation [50, 51]. The GSH-consuming capacity of FeNC was demonstrated using a 5,5’-dithiobis-(2-nitrobenzoic acid) (DTNB) indicator, which could interact with GSH to produce TNB (Fig. S16). As expected, the absorbance peak at 412 nm of TNB decreased gradually with the concentration of FeNC (Fig. 4f). Even in neutral buffer solution (PBS buffer, pH = 7.4), FeNC group also exhibited a significantly decreased than N-C group and Fe@ZIF-8 group (Fig S10d). All these results revealed the GSHOx-like activity of FeNC. Furthermore, the stability of the quadruple enzyme-like activities of FeNC was demonstrated in Fig. S17.

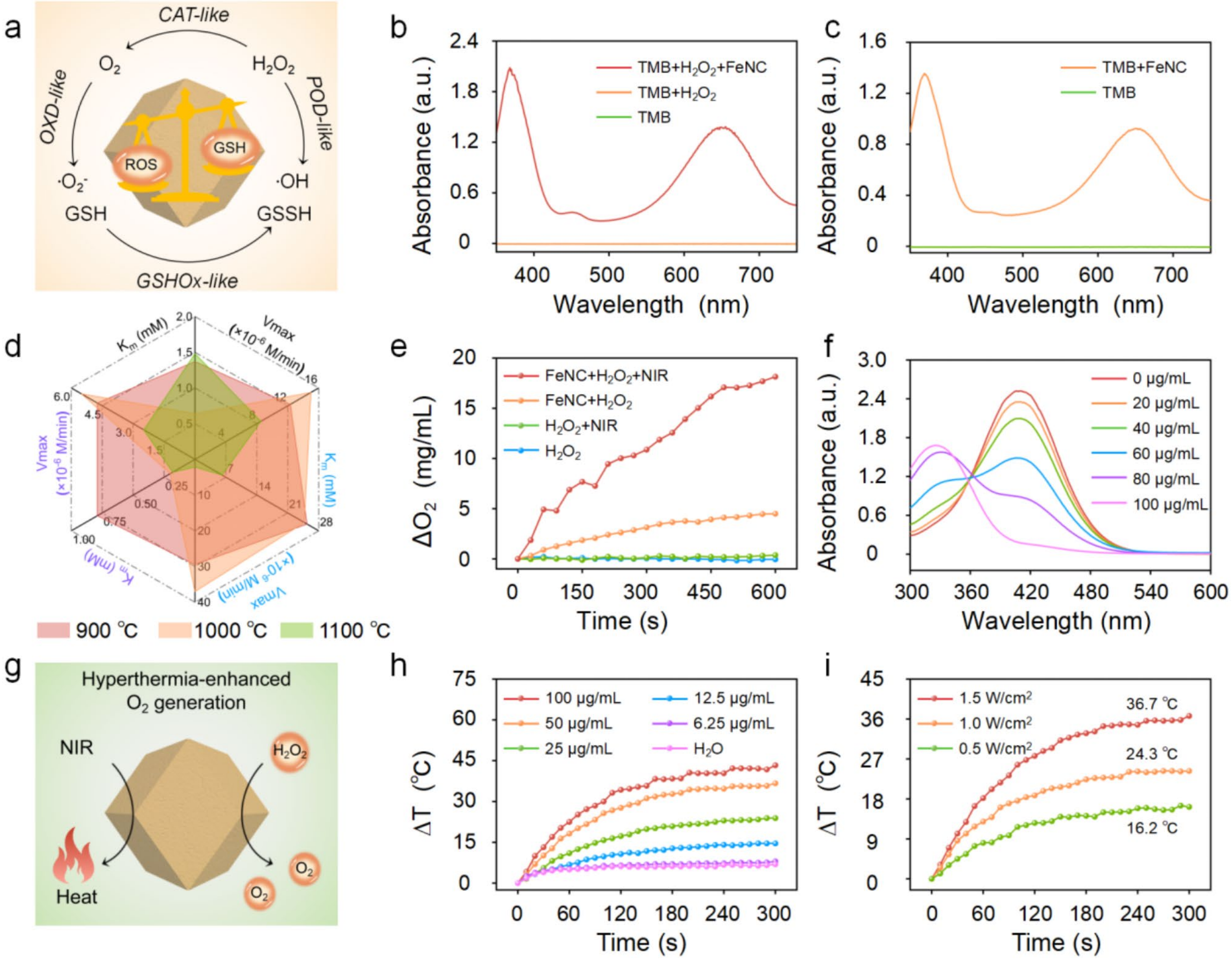

Fig. 4 The multienzyme activity and photothermal performance of FeNC. (**a**) Schematic presentation of multienzyme catalytic activities of FeNC. The TMB assay for (**b**) POD-mimic and (**c**) OXD-mimic activities of FeNC. (**d**) Michaelis-Menten kinetic analysis of FeNC pyrolysis under 900 ℃, 1000 ℃, and 1100 ℃, respectively. The black-marked K_m and V_{max} represented POD-like activity with TMB as a substrate. The blue-marked K_m and V_{max} represented POD-like activity with H_2O_2 as a substrate. The purple-marked K_m and V_{max} represented OXD-like activity with TMB as a substrate. (**e**) O_2 generation of FeNC under different treatments. (**f**) GSH depletion after treatment with different concentrations of FeNC. (**g**) Schematic image of hyperthermia-enhanced O_2 generation. (**h**) Temperature change of H_2O and FeNC aqueous at different concentrations irradiated by laser (808 nm, 1 W/cm^2). (**i**) Temperature change of aqueous (50 μg/mL) irradiated by laser (808 nm) with different power densities

In vitro anticancer effect and potential mechanism of FeNC-FA

The synergistic therapeutic mechanism of FeNC-FA in mouse breast cancer cells (4T1) was exhibited in Fig. 5g. To endow the FeNC with cancer cells targeting ability, folic acid (FA) was modified by electrostatic adsorption. A UV-vis characterization peak of FA at 250 nm was observed in FeNC-FA (Fig. S18a). The Zeta potential also confirmed the successful fabrication of FeNC-FA (Fig. S18b). The stability of FeNC-FA was investigated in PBS buffers with different pH values (7.4 and 6.4). The zeta potential of FeNC-FA all exhibited negligible changes within 12 h (Fig. S19). The uptake behaviors of 4T1 cells were first explored using confocal laser scanning microscopy (CLSM). As shown in Fig. 5a, the red fluorescence signals were gradually increased with the incubation time, and the brightest fluorescence was obtained at 6 h in the FeNC-FA group, while only a slight fluorescence signals were observed in the FeNC group. The result demonstrated the FeNC-FA with excellent compatibility could be internalized efficiently by 4T1 cells.

The cytotoxicity of FeNC-FA was evaluated by Cell Counting Kit-8 (CCK-8) assay. Compared with normal mouse fibroblast L929 cells, the FeNC-FA showed a significant inhibitory effect on 4T1 cells (Fig. 5b). Moreover, the FeNC-FA + H_2O_2 group showed a stronger killing ability due to mimicked tumor microenvironment. The synergistic therapeutic effect was proved in Fig. 5c and 18.37% of cells died when they were incubated with FeNC-FA + H_2O_2 + NIR group.

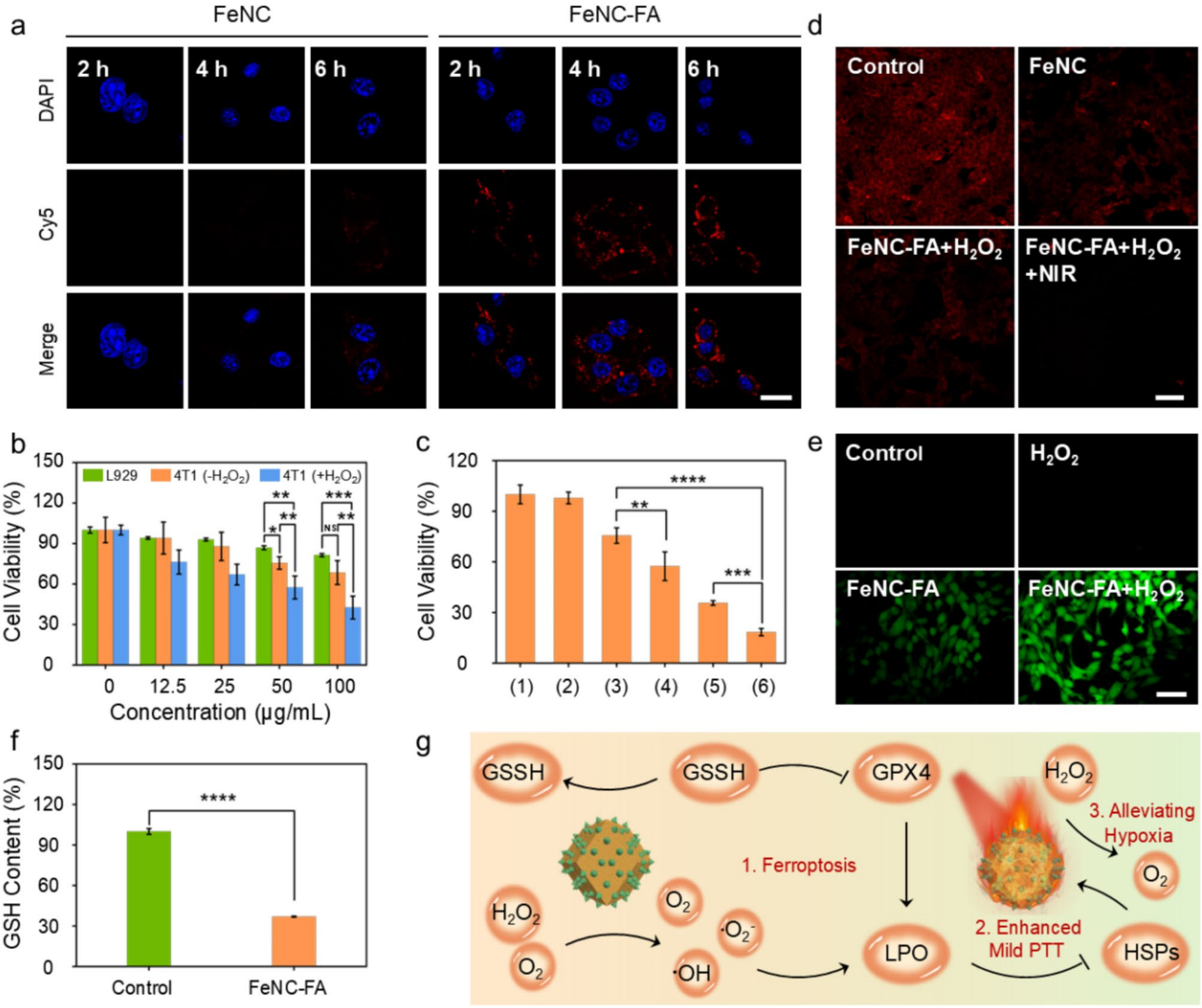

Fig. 5 In vitro anticancer effect and potential mechanism of FeNC-FA. (**a**) The cellular uptake behavior of FeNC and FeNC-FA (Scale bar is 20 μm). (**b**) Cytotoxicity assays of L929 cells and 4T1 cells treated with different concentration of FeNC-FA. (**c**) Cytotoxicity assays of 4T1 cells after different treatments. Group 1 to 6 were Control, NIR, FeNC-FA (50 μg/mL), FeNC-FA (50 μg/mL) + H_2O_2 (100 μM), FeNC-FA (50 μg/mL) + NIR, and FeNC-FA(50 μg/mL) + H_2O_2 (100 μM) + NIR. CLSM image of intracellular (**d**) O_2 generation and (**e**) ROS level after various treatments (Scale bars are 100 μm and 50 μm, respectively). (**f**) Intracellular GSH level after different treatments. (**g**) Schematic illustration of FeNC-FA triggering synergistic therapeutic mechanism. $^*P < 0.05$; $^{**}P < 0.01$; and $^{***}P < 0.001$; $^{****}P < 0.0001$; and ns: not significant

To investigate the FeNC-induced ferroptosis pathway, the intracellular ROS levels were investigated with different treatments by 2,7-dichlorofluorescein diacetate (DCFH-DA) probe, which could be oxidized by intracellular ROS and produced 2,7-dichlorofluorescein (DCF) with green fluorescence signal [52]. Compared with the PBS buffer and H_2O_2 treated groups, the FeNC-FA treated group exhibited a significant green fluorescence. Importantly, the FeNC-FA + H_2O_2 treated group showed a brighter fluorescence due to the H_2O_2 supplement in the culture medium (Fig. 5e). The intracellular O_2 was monitored using $[Ru(dpp)_3]Cl_2$ as the probe, and the red fluorescence signal was decreased in the FeNC-FA + H_2O_2 group and a more sufficient O_2 generation was observed in the FeNC-FA + H_2O_2 + NIR group (Fig. 5d). It is worth noting that the fluorescence signal of the $[Ru(dpp)_3]Cl_2$ probes remained unchanged under a NIR irradiation alone (Fig. S20). Then, we further investigated the GSH depletion capacity of FeNC-FA. As shown in Fig. 4f, 100 μg/mL of FeNC-FA could consume nearly 64% of GSH. The deactivation of GSH-related GPX4 was explored in Fig. S21, and its activity was greatly reduced under FeNC-FA + H_2O_2 treatment. Further, the regulatory effects of ferroptosis on mPTT were investigated. As expected, the expression of HSP70 was dramatically down-regulated in the FeNC-FA + H_2O_2 group (Fig. S21).

In vivo PA and photothermal imaging

The PA and photothermal imaging abilities of FeNC-FA were explored on 4T1-tumor-bearing mice. The PA signals of FeNC-FA in mice were monitored at different time intervals. The PA signals at the tumor site showed remarkable time-dependent enhancement after intravenous injection (Fig. 6a and b). After 6 h, it reached the maximum via the FA target and EPR effect, which showed a 7.02-fold enhancement compared to that of pre-injection. As time progressed, it gradually decreased due to metabolism. These results indicated that FeNC-FA preferentially accumulates in tumor tissues, and 6 h after intravenous injection was the optimal treatment time.

The temperature changes were recorded by an infrared thermal imaging instrument. After the 4T1-tumor-bearing mice were intravenously injected with FeNC-FA and PBS buffer (10 mM, pH = 7.4) for 6 h, the neoplastic areas of mice were irradiated with laser (808 nm) for 10 min, respectively. The temperature of tumor site displayed a distinct increase in the FeNC-FA group compared to the PBS buffer treatment (Fig. 6c and d), which was reached approximately 43 ℃ after irradiation for 4 min and kept the temperature constant after irradiation for another 6 min. These results confirmed that the FeNC-FA could realize the required mPTT in mice.

Biological safety evaluation

The biosecurity of FeNC-FA in vivo was evaluated via serum biochemistry assay. Different markers including liver function indexes, renal function indexes, and blood routine indexes were monitored at different point time after intravenously injected with FeNC-FA (Fig. S22). All the indicators showed no significant changes compared to 0 days, indicating the FeNC-FA treatment exhibited no negative impact on the serum biochemistry. Additionally, hemolysis analysis indicated inconspicuous hemolysis reactions, even at a high dose of 200 μg/mL (Fig. S23), suggesting a satisfactory hemocompatibility of FeNC-FA.

In vivo therapeutic evaluation of FeNC-FA

The therapeutic potential of FeNC-FA was further assessed in 4T1-tumor-bearing mice. When the tumor volumes reached approximately 80–100 mm^3, the mice were randomly assigned to four groups ($n = 6$ per group): (1) control, (2) NIR, (3) FeNC-FA, and (4) FeNC-FA + NIR. Subsequently, the tumor sizes and body weights of mice were recorded every two days. The FeNC-FA with NIR laser irradiation (808 nm, 0.5 W/cm^2, 10 min) exhibited the most remarkable tumor growth inhibition (Fig. 7a and b, Fig. S24) and smallest tumor weight (Fig. 7c) among all the groups, owing to the synergistic effects of catalytic therapy and mPTT. All the mice that received different treatments showed a negligible variation in body weight (Fig. 7d), suggesting

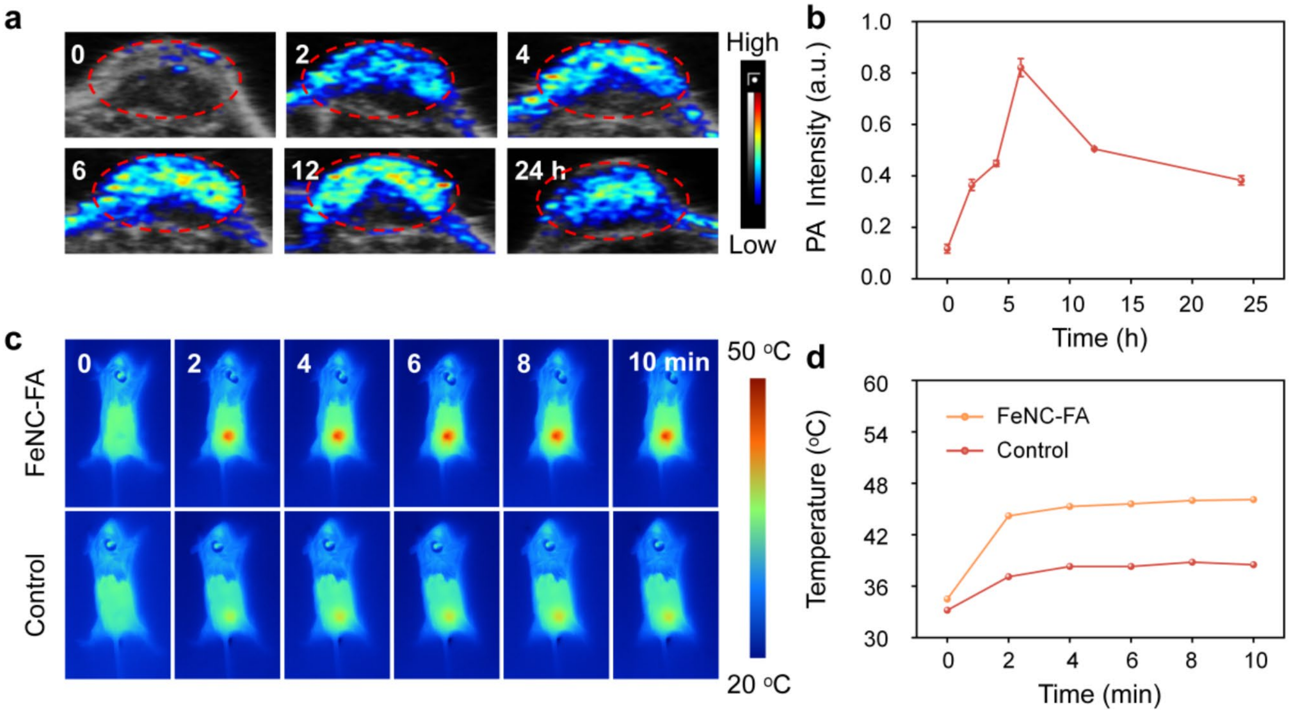

Fig. 6 PA and Photothermal imaging of FeNC-FA in vivo. (**a**) in vivo PA images and (**b**) corresponding intensity values of FeNC-FA of tumor region after intravenous injection. (**c**) Infrared thermal images and (**d**) corresponding temperature changes of tumor region exposed to NIR laser (808 nm, 0.5 W/cm^2) for consecutive 10 min after intravenous injection of PBS buffer (control) and FeNC-FA for 6 h

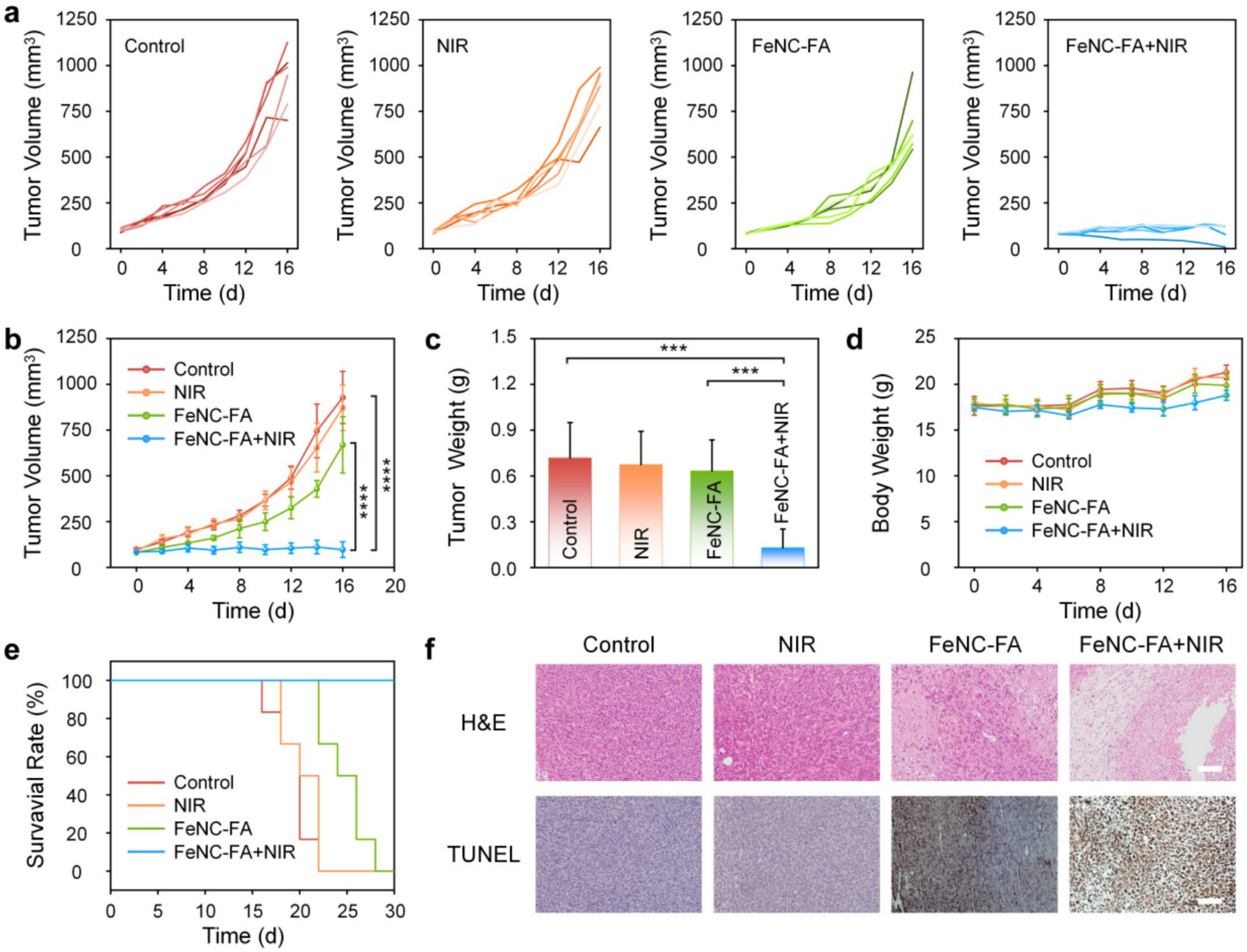

Fig. 7 In vivo anti-tumor assessment of FeNC-FA. (**a**-**b**) Tumor volume curves, (**c**) Tumor weight, (**d**) Body weight, and (**e**) Survival percentages of mice after different treatments (***$P < 0.001$, ****$P < 0.0001$). (**f**) H&E and TUNEL staining of tumor tissues harvested from the different groups after 16 d treatments (Scale bar is 100 μm)

no significant toxicity of the injected FeNC-FA during the treatment process. The collected tumors of each group were sliced into sections for immunohistochemical evaluation. The hematoxylin and eosin (H&E) staining of tumor sections displayed that the FeNC-FA + NIR treatment group exhibited the most severe damage. Similar results were revealed in terminal-deoxynucleotidyl transferase-mediated deoxyuridine triphosphate nick end labeling (TUNEL) analysis (Fig. 7f). The H&E staining analysis of the major organs was performed in Fig. S25, further indicating the good biocompatibility of FeNC-FA with NIR irradiation. Moreover, tumor-bearing mice survived after 30 days of treatment in group 4, which showed a markedly prolonged lifetime than the other three groups (Fig. 7e), further demonstrating superior anticancer efficacy.

Conclusion

In summary, we rationally fabricated a FA-functionalized Fe-dependent nanozyme (FeNC-FA) with multiple enzyme-like activities, that is, POD, OXD, CAT, and GSHOx, for mutually reinforced catalytic and mild photothermal anticancer treatment. We first comprehensively characterized single-atom FeNC-FA with a Fe-N_4 catalytic center, which could simultaneously produce ROS and deplete GSH in TME to perturb the redox adaptation and induce ferroptosis. Under an 808 nm laser irradiation, the FeNC-FA could also serve on the photothermal material and realize an approving mPTT for tumor regression, benefiting from the effective destruction of HSP during ferroptosis. Meanwhile, the photothermal effect could boost O_2 generation and relieve the hypoxia in TME. In vivo therapy, an excellent PA imaging ability of FeNC-FA was demonstrated, which provided an intelligent exemplification for reliable tumor treatment. Thus, such unique FeNC-FA realized a PA imaging-guided catalytic and mild photothermal synergistic therapy, which provided a promising personalized candidate for cancer theranostics in the future.

Despite the exceptional catalytic properties of FeNC with its Fe-N_4 catalytic center, there still exist improvement. For example, heterogeneous dual atoms-doping on a carbon can introduce a more abundant array of active sites, thereby enhancing significantly its catalytic activity. We will developed a series of dual atoms-doping nanozymes and further investigated their anticancer effects.

Supplementary Information

The online version contains supplementary material available at https://doi.org/10.1186/s12951-025-03320-2.

Supplementary Material 1

Acknowledgements
The authors acknowledge the Medical Experimental Center of Shanxi Bethune Hospital for providing the necessary equipment for this work.

Author contributions
F.Y., CY.Y. and NN.L. designed the work, wrote the main manuscript text and executed all the experiments. XX.J. participated the cell experiments and H&E and TUNEL staining assays. BJ.D. and PR.B. participated and analyzed WB experiments. LP.L. and RP.Z. reviewed and edited the manuscript.

Funding
This work has been financially supported by the National Key R&D Program of China (2023YFC3402800), National Natural Science Foundation of China (No: 82120108016, 82071987, U22A20349, 22204094); the Central Government Guided Local Science and Technology Development Fund Research Project (YDZJSX20231A055); Key Laboratory of Nano-imaging and Drug-loaded Preparation of Shanxi Province (No. 202104010910010); Shanxi Province Science Foundation for Youths (202103021223230, 202103021223405); Research project of Health Commission of Shanxi Province (No. 2022137); Shanxi Province Higher Education Institutions' Young Academic Leadership Program (No. 2024Q012); Science Research Start-up Fund for Doctor of Shanxi Medical University (XD2108).

Data availability
No datasets were generated or analysed during the current study.

Declarations

Ethics approval and consent to participate
All animal experiments were approved by Ethics Committee of Shanxi Medical University.

Consent for publication
All authors consent to publish.

Competing interests
The authors declare no competing interests.

Received: 21 November 2024 / Accepted: 11 March 2025

References

1. Liu J, Dong S, Gai S, Dong Y, Liu B, Zhao Z, Xie Y, Feng L, Yang P, Lin J. Design and mechanism insight of monodispersed AuCuPt alloy nanozyme with antitumor activity. ACS Nano. 2023;17(20):20402–23.
2. Jana D, Wang D, Bindra AK, Guo Y, Liu J, Zhao Y. Ultrasmall alloy nanozyme for ultrasound- and near-infrared light-promoted tumor ablation. ACS Nano. 2021;15(4):7774–82.
3. Liu Y, Wang B, Zhu J, Xu X, Zhou B, Yang Y. Single-atom nanozyme with asymmetric electron distribution for tumor catalytic therapy by disrupting tumor redox and energy metabolism homeostasis. Adv Mater. 2023;35(9):2208512.
4. Lin S, Ze H, Zhang XG, Zhang YJ, Song J, Zhang H, Zhong HL, Yang ZL, Yang C, Li JF et al. Direct and simultaneous identification of multiple mitochondrial reactive oxygen species in living cells using a SERS borrowing strategy. Angew Chem Int Ed 2022, 61 (25), e202203511.
5. Wang D, Wu H, Phua SZF, Yang G, Qi Lim W, Gu L, Qian C, Wang H, Guo Z, Chen H, et al. Self-assembled single-atom nanozyme for enhanced photodynamic therapy treatment of tumor. Nat Commun. 2020;11(1):357.
6. Liu C, Cao Y, Cheng Y, Wang D, Xu T, Su L, Zhang X, Dong H. An open source and reduce expenditure ROS generation strategy for chemodynamic/photodynamic synergistic therapy. Nat Commun. 2020;11(1):1735.
7. Chen Z, Liu Z, Zhou Y, Rao K, Lin J, Zhu D, Ning S, Wang H. Bionic aggregation-induced emission photosensitizer for enhanced cancer immunotherapy. Mater Today Bio. 2024;28:101217.
8. Ning S, Lyu M, Zhu D, Lam JWY, Huang Q, Zhang T, Tang BZ. Type-I AIE photosensitizer loaded biomimetic system boosting cuproptosis to inhibit breast cancer metastasis and rechallenge. ACS Nano. 2023;17(11):10206–17.
9. Chen H, Luo X, Huang Q, Liu Z, Lyu M, Chen D, Mo J, Zhu D. Platelet membrane fusion liposome loaded with type I AIE photosensitizer to induce chemoresistance cancer pyroptosis and immunogenic cell death for enhancing cancer immunotherapy. Chem Eng J. 2023;476:146276.
10. Liang S, Deng X, Xu G, Xiao X, Wang M, Guo X, Ma Pa, Cheng Z, Zhang D, Lin J. A novel Pt-TiO_2 heterostructure with oxygen-deficient layer as bilaterally enhanced sonosensitizer for synergistic chemo-sonodynamic cancer therapy. Adv Funct Mater. 2020;30(13):1908598.
11. Pan X, Wang W, Huang Z, Liu S, Guo J, Zhang F, Yuan H, Li X, Liu F, Liu H. MOF-derived double-layer hollow nanoparticles with oxygen generation ability for multimodal imaging-guided sonodynamic therapy. Angew Chem Int Ed. 2020;59(32):13557–61.
12. Wen D, Li K, Deng R, Feng J, Zhang H. Defect-rich glassy $IrTe_2$ with dual enzyme-mimic activities for sono-photosynergistic-enhanced oncotherapy. J Am Chem Soc. 2023;145(7):3952–60.
13. Wang X, Zhong X, Bai L, Xu J, Gong F, Dong Z, Yang Z, Zeng Z, Liu Z, Cheng L. Ultrafine titanium monoxide (TiO_{1+x}) nanorods for enhanced sonodynamic therapy. J Am Chem Soc. 2020;142(14):6527–37.
14. Xu B, Li S, Zheng L, Liu Y, Han A, Zhang J, Huang Z, Xie H, Fan K, Gao L, et al. A bioinspired five-coordinated single-atom iron nanozyme for tumor catalytic therapy. Adv Mater. 2022;34(15):2107088.
15. Wang X, Ren X, Yang J, Zhao Z, Zhang X, Yang F, Zhang Z, Chen P, Li L, Zhang R. Mn-single-atom nano-multizyme enabled NIR-II photoacoustically monitored, photothermally enhanced ROS storm for combined cancer therapy. Biomaterials Res. 2023;27(1):125.
16. Gao F, Shao T, Yu Y, Xiong Y, Yang L. Surface-bound reactive oxygen species generating nanozymes for selective antibacterial action. Nat Commun. 2021;12(1):745.
17. Wang Z, Zhang Y, Ju E, Liu Z, Cao F, Chen Z, Ren J, Qu X. Biomimetic nanoflowers by self-assembly of nanozymes to induce intracellular oxidative damage against hypoxic tumors. Nat Commun. 2018;9(1):3334.
18. Wang B, Khoshfetrat SM, Mohamadimanesh H. Peroxidase-like manganese oxide nanoflowers-delaminated Ti_3C_2 MXene for ultrasensitive dual-mode and real-time detection of H_2O_2 released from cancer cells. Microchem J. 2024;207:111796.
19. Momeni F, Khoshfetrat SM, Bagheri H, Zarei K. Ti_3C_2 MXene-based nanozyme as coreaction accelerator for enhancing electrochemiluminescence of glucose biosensing. Biosens Bioelectron. 2024;250:116078.
20. Khoshfetrat SM, Chegeni I. Rational design of Ti_3C_2 MXene nanocomposite with bromophenol blue for efficient signal amplification: sensitive electrochemical detection of cardiac troponin I in patient plasma. Sens Actuators B. 2023;397:134668.
21. Khoshfetrat SM, Nabavi M, Mamivand S, Wang Z, Wang Z, Hosseini M. Ionic liquid-delaminated Ti_3C_2 MXene nanosheets for enhanced electrocatalytic oxidation of tryptophane in normal and breast cancer serum. Microchim Acta. 2025;192(2):113.
22. Khoshfetrat SM, Fasihi K, Moradnia F, Kamil Zaidan H, Sanchooli EA. Label-free multicolor colorimetric and fluorescence dual mode biosensing of HIV-1 DNA based on the bifunctional $NiFe_2O_4$@UiO-66 nanozyme. Anal Chim Acta. 2023;1252:341073.

23. Li Z, Ding B, Li J, Chen H, Zhang J, Tan J, Ma X, Han D, Ma Pa, Lin J. Multi-enzyme mimetic MoCu dual-atom nanozyme triggering oxidative stress cascade amplification for high-efficiency synergistic cancer therapy. Angew Chem Int Ed 2024, 64 (1), e202413661.
24. Zhao R, Zhu Y, Feng L, Liu B, Hu Y, Zhu H, Zhao Z, Ding H, Gai S, Yang P. Architecture of vanadium-based MXene dysregulating tumor redox homeostasis for amplified nanozyme catalytic/photothermal therapy. Adv Mater. 2023;36(2):2307115.
25. Ai Y, Hu ZN, Liang X, Sun Hb, Xin H, Liang Q. Recent advances in nanozymes: from matters to bioapplications. Adv Funct Mater. 2021;32(14):2110432.
26. Zhang N, Ping W, Xiang J, Chu S, Li D, Ning S, Zhu D, Zeng W, Xu Q. Biomimetic single-atom nanozyme for dual starvation-enhanced breast cancer immunotherapy. Adv Healthc Mater. 2024;14:2401362.
27. Zhang R, Jiang B, Fan K, Gao L, Yan X. Designing nanozymes for in vivo applications. Nat Rev Bioeng. 2024;2(10):849–68.
28. Wu L, Lin H, Cao X, Tong Q, Yang F, Miao Y, Ye D, Fan Q. Bioorthogonal Cu single-atom nanozyme for synergistic nanocatalytic therapy, photothermal therapy, cuproptosis and immunotherapy. Angew Chem Int Ed. 2024; 63 (27): e202405937.
29. Guo Z, Hong J, Song N, Liang M. Single-atom nanozymes: from precisely engineering to extensive applications. Acc Chem Res. 2024;5(3):347–57.
30. Han J, Guan J. Applications of single-site iron nanozymes in biomedicine. Coord Chem Rev. 2023;490:215209.
31. Jiang B, Duan D, Gao L, Zhou M, Fan K, Tang Y, Xi J, Bi Y, Tong Z, Gao GF, et al. Standardized assays for determining the catalytic activity and kinetics of peroxidase-like nanozymes. Nat Protoc. 2018;13(7):1506–20.
32. Zhu X, Wu J, Liu R, Xiang H, Zhang W, Chang Q, Wang S, Jiang R, Zhao F, Li Q, et al. Engineering single-atom iron nanozymes with radiation-enhanced self-cascade catalysis and self-supplied H_2O_2 for radio-enzymatic therapy. ACS Nano. 2022;16(11):18849–62.
33. Cao F, Sang Y, Liu C, Bai F, Zheng L, Ren J, Qu X. Self-adaptive single-atom catalyst boosting selective ferroptosis in tumor cells. ACS Nano. 2022;16(1):855–68.
34. Liu H, Jiang S, Li M, Lei S, Wu J, He T, Wang D, Lin J, Huang P. Dual enzyme-driven cascade reactions modulate immunosuppressive tumor microenvironment for catalytic therapy and immune activation. ACS Nano. 2024;18(44):30345–59.
35. Gao G, Sun X, Liang G. Nanoagent-promoted mild-temperature photothermal therapy for cancer treatment. Adv Funct Mater. 2021;31(25):2100738.
36. Dong S, Dong Y, Zhao Z, Liu J, Liu S, Feng L, He F, Gai S, Xie Y, Yang P. Electron transport chain interference strategy of amplified mild-photothermal therapy and defect-engineered multi-enzymatic activities for synergistic tumor-personalized suppression. J Am Chem Soc. 2023;145(17):9488–507.
37. Chang M, Hou Z, Wang M, Wen D, Li C, Liu Y, Zhao Y, Lin J. Cu single atom nanozyme based high-efficiency mild photothermal therapy through cellular metabolic regulation. Angew Chem Int Ed 2022;61 (50): e202209245.
38. Wang Q, Ina T, Chen W-T, Shang L, Sun F, Wei S, Sun-Waterhouse D, Telfer SG, Zhang T, Waterhouse G. I. N. Evolution of Zn(II) single atom catalyst sites during the pyrolysis-induced transformation of ZIF-8 to N-doped carbons. Sci Bull. 2020;65(20):1743–51.
39. Han J, Meng X, Lu L, Bian J, Li Z, Sun C. Single-atom Fe-N_x-C as an efficient electrocatalyst for zinc-air batteries. Adv Funct Mater. 2019;29(41):1808872.
40. Khoshfetrat SM, Mehrgardi MA. Amplified electrochemical genotyping of single-nucleotide polymorphisms using a graphene-gold nanoparticles modified glassy carbon platform. RSC Adv. 2015;5(37):29285–93.
41. Khoshfetrat SM, Mamivand S, Darband GB. Hollow-like three-dimensional structure of methyl orange-delaminated Ti_3C_2 MXene nanocomposite for high-performance electrochemical sensing of tryptophan. Microchim Acta. 2024;191(9):546.
42. Khoshfetrat SM, Moradi M, Zhaleh H, Hosseini M. Multifunctional methyl orange-delaminated Ti_3C_2 MXene for non-enzymatic/metal-free electrochemical detection of hydrogen peroxide and hydrazine. Microchem J. 2024;205:111382.
43. Liu W, Chen Q, Wu J, Zhang F, Han L, Liu J, Zhang H, Hao Z, Shi E, Sun Y, et al. Asymmetric coordination of iron single-atom nanozymes with efficient self-cascade catalysis for ferroptosis therapy. Adv Funct Mater. 2023;34(14):2312308.
44. Chen D, Xia Z, Guo Z, Gou W, Zhao J, Zhou X, Tan X, Li W, Zhao S, Tian Z, et al. Bioinspired porous three-coordinated single-atom Fe nanozyme with oxidase-like activity for tumor visual identification via glutathione. Nat Commun. 2023;14(1):7127.
45. Liu W, Shi E, Wu H, Liang Y, Chen M, Zhang H, Zhang R, Li X, Wang Y, Zhang L. Spatially axial boron coordinated single-atom nanozymes with boosted multi-enzymatic performances for periodontitis treatment. Adv Funct Mater. 2024;34(39):2403386.
46. Zeng R, Li Y, Hu X, Wang W, Li Y, Gong H, Xu J, Huang L, Lu L, Zhang Y, et al. Atomically site synergistic effects of dual-atom nanozyme enhances peroxidase-like properties. Nano Lett. 2023;23(13):6073–80.
47. Jiang Z, Liu X, Liu XZ, Huang S, Liu Y, Yao ZC, Zhang Y, Zhang QH, Gu L, Zheng LR, et al. Interfacial assembly of binary atomic metal-N_x sites for high-performance energy devices. Nat Commun. 2023;14(1):1822.
48. Wei S, Sun Y, Qiu Y-Z, Li A, Chiang C-Y, Xiao H, Qian J, Li Y. Self-carbon-thermal-reduction strategy for boosting the Fenton-like activity of single Fe-N_4 sites by carbon-defect engineering. Nat Commun. 2023;14(1):7549.
49. Khoshfetrat SM, Hashemi P, Afkhami A, Hajian A, Bagheri H. Cascade electrochemiluminescence-based integrated graphitic carbon nitride-encapsulated metal-organic framework nanozyme for prostate-specific antigen biosensing. Sens Actuators B. 2021;348:130658.
50. Nakamura T, Conrad M. Exploiting ferroptosis vulnerabilities in cancer. Nat Cell Biol. 2024;26(9):1407–19.
51. Dong Z, Liang P, Guan G, Yin B, Wang Y, Yue R, Zhang X, Song G. Overcoming hypoxia-induced ferroptosis resistance via a^{19}F/^{1}H-MRI traceable core-shell nanostructure. Angew Chem Int Ed. 2022, 61 (48), e202206074.
52. Zhao Z, Dong S, Liu Y, Wang J, Ba L, Zhang C, Cao X, Wu C, Yang P. Tumor microenvironment-activable manganese-boosted catalytic immunotherapy combined with PD-1 checkpoint Blockade. ACS Nano. 2022;16(12):20400–18.

Publisher's note